

Nucleation of highly dense nanoscale precipitates based on warm laser shock peening

Yiliang Liao, Chang Ye, Bong-Joong Kim, Sergey Suslov, Eric A. Stach, and Gary J. Cheng

Citation: *Journal of Applied Physics* **108**, 063518 (2010); doi: 10.1063/1.3481858

View online: <http://dx.doi.org/10.1063/1.3481858>

View Table of Contents: <http://scitation.aip.org/content/aip/journal/jap/108/6?ver=pdfcov>

Published by the [AIP Publishing](#)

Articles you may be interested in

[Experiment investigation on microstructure and mechanical properties of TC17 titanium alloy treated by laser shock peening with different laser fluence](#)

J. Laser Appl. **25**, 042001 (2013); 10.2351/1.4800444

[Microstructure and vacancy-type defects of high-pressure torsion deformed Al-3wt%Cu alloy](#)

J. Appl. Phys. **112**, 103506 (2012); 10.1063/1.4765034

[Microstructure and mechanical properties of copper subjected to cryogenic laser shock peening](#)

J. Appl. Phys. **110**, 083504 (2011); 10.1063/1.3651508

[Dislocation pinning effects induced by nano-precipitates during warm laser shock peening: Dislocation dynamic simulation and experiments](#)

J. Appl. Phys. **110**, 023518 (2011); 10.1063/1.3609072

[Precipitation and high temperature magnetic properties of FeCo-based alloys](#)

J. Appl. Phys. **97**, 053905 (2005); 10.1063/1.1857057



Not all AFMs are created equal
Asylum Research Cypher™ AFMs
There's no other AFM like Cypher

www.AsylumResearch.com/NoOtherAFMLikeIt

OXFORD
INSTRUMENTS
The Business of Science®

Nucleation of highly dense nanoscale precipitates based on warm laser shock peening

Yiliang Liao,¹ Chang Ye,¹ Bong-Joong Kim,² Sergey Suslov,² Eric A. Stach,² and Gary J. Cheng^{1,a)}

¹*School of Industrial Engineering, Purdue University, West Lafayette, IN 47906, USA*

²*School of Materials Science and Engineering, Purdue University, West Lafayette, IN 47906, USA*

(Received 3 June 2010; accepted 24 July 2010; published online 21 September 2010)

Warm laser shock peening (WLSP) is an innovative thermomechanical processing technique, which combines the advantages of laser shock peening (LSP) and dynamic aging (DA). It has been found that a unique microstructure with highly dense nanoscale precipitates surrounded by dense dislocation structures is generated by WLSP. In order to understand the nucleation mechanism of the highly dense precipitates during WLSP, aluminum alloy 6061 (AA6061) has been used by investigating the WLSP process with experiments and analytical modeling. An analytical model has been proposed to estimate the nucleation rate in metallic materials after WLSP. The effects of the processing temperature and high strain rate deformation on the activation energy of nucleation have been considered in this model. This model is based on the assumption that DA during WLSP can be assisted by the dense dislocation structures and warm temperature. The effects of the working temperature and dislocation density on the activation energy of precipitation have been investigated. This model is validated by a series of experiments and characterizations after WLSP. The relationships between the processing conditions, the nucleation density of precipitates and the defect density have been investigated. © 2010 American Institute of Physics. [doi:10.1063/1.3481858]

I. INTRODUCTION

Laser shock peening (LSP) is one of the most effective material processing techniques used to introduce compressive residual stresses and the work hardening on the surfaces of metallic materials, in order to improve the fatigue life and wear resistance.^{1–3} There have been extensive investigations on LSP seeking to understand the generation of shock waves, the interaction between stress waves and metallic materials, and how compressive residual stresses and plastic deformations are produced in metallic targets. However, few researches have taken into account the effects of the elevated working temperature on LSP process.

Nonetheless, the effects of the warm temperature on plastic deformation have been investigated in many other manufacturing processes. It is reported by Wick *et al.*⁴ that the elevated temperature in shot peening results in the improved stability of the residual stress due to dynamic aging (DA). DA is an integrated process combining the thermomechanical processing and the age hardening treatment to introduce highly dense precipitates in metallic materials. Conventional static aging is a slow process, in which the nucleation and growth of precipitates take place after the deformation, while DA is a much faster process in which the precipitation occurs simultaneously during the deformation process. DA is affected significantly by the processing temperature and applied strain rate. It is found by Gündüz⁵ that the ultimate tensile stress and initial work hardening rates in microalloyed steels can be improved significantly as results of DA.

It is reported by Jiang *et al.*⁶ that in creep-fatigue tests of 316L stainless steel, the DA pretreatment can postpone the cycle at the first abrupt displacement and effectively prolong the steel's fatigue life.

Warm LSP (WLSP) is an innovative thermomechanical processing technique developed recently in our research group, which takes the advantages of both LSP and DA.⁷ The strain rate and the resulted dislocation density of LSP is the highest among all the plastic deformation process. One of the most promising characteristics of WLSP is that a unique microstructure with highly dense nanoscale precipitates surrounded by dense dislocation structures can be generated. In WLSP process, the nucleation and growth rate of precipitates are affected by the processing temperature and the applied laser power intensity. Since the generation of highly dense precipitates plays the key role in improving material's mechanical properties using WLSP, it is worthwhile investigating the fundamental mechanism of the nucleation of precipitates in WLSP process.

In this study, aluminum alloy 6061 (AA6061) is chosen to study the WLSP process. The microstructures after WLSP are characterized by transmission electron microscopy (TEM) and x-ray diffraction (XRD). A mathematical model is developed to predict the nucleation density of precipitates in WLSP. The effects of the working temperature and dislocation density on the activation energy of precipitation are investigated. The modeling results are compared with a series of experiments and characterizations after WLSP. The relationships between the processing conditions, the nucleation density of precipitates, and the defect density are discussed.

^{a)}Electronic mail: gjcheng@purdue.edu.

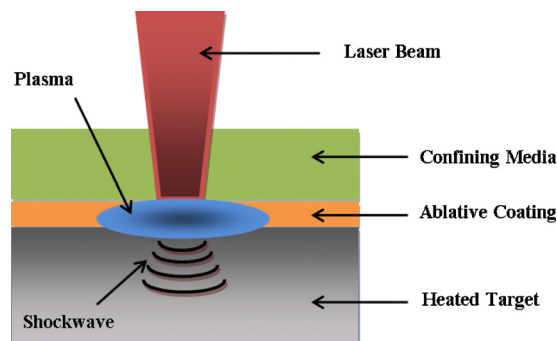


FIG. 1. (Color online) The schematic view of the WLSP process.

II. EXPERIMENT

The material used in this study is AA6061 alloy, having the following chemical composition in weight percent: Mg—0.92, Si—0.76, Fe—0.28, Cu—0.22, Ti—0.10, Cr—0.07, Zn—0.06, Mn—0.04, Be—0.003, V—0.01, and Al—balance. AA6061 plates with a thickness of 3.0 mm (from McMaster-Carr Supply) are used for WLSP experiments. Aluminum foils with a uniform thickness of 30 μm are used as an ablative coating material. The foil is firmly attached to the sample surface by the vacuum grease. Instead of water, BK7 glass is used as the confinement media. BK7 glass has a higher shock impedance, which results in a higher peak plasma pressure. In addition, water is not suitable for WLSP processing due to its low evaporation temperature, while glass has no such issue. Note that for the industrial applications of WLSP, the silicone oil with a flash point over 600 $^{\circ}\text{F}$ is more practical as a confinement media than the glass, since the glass can be shattered by the laser-induced shock pressure. A schematic view of WLSP process is shown in Fig. 1. A hot plate placed below the sample fixture is used to increase the working temperature during WLSP. The temperature is monitored by a digital scientific thermometer. A Q-switched Nd-YAG laser (Surelite III from Continuum, Inc.), operating at a wavelength of 1064 nm with a pulse width of 5 ns is used to deliver the laser energy. The laser beam diameter is 1 mm. The laser power intensity is changed by adjusting the Q-switched delay time.

III. MICROSTRUCTURE STUDY AFTER WLSP

In this work, TEM (FEI-Tecnaï TEM and FEI-Titan TEM operated at 200 kV and 300 kV, respectively) is used to study the microstructures in AA6061 after WLSP. To prepare the TEM sample, a thin layer of the sample surface after WLSP is sectioned by a diamond saw. The final thinning is carried out by the H-Bar method using the focus ion beam (Nova-200). Before TEM observations, the sample is cleaned in acetone to get rid of the contaminants from the ion beam.

The dark field (DF) TEM images in Fig. 2 show the dislocation and precipitate structures of AA6061 after WLSP at 160 $^{\circ}\text{C}$. It can be seen that the highly dense dislocations and precipitates are entangled together in both the T6 condition sample [Fig. 2(a)] and the solutionized sample [Fig. 2(b)]. This reveals that precipitates are more likely to nucleate around the dislocations during DA, while the movement

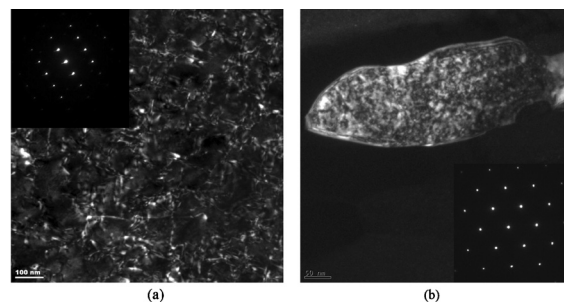


FIG. 2. DF TEM images showing microstructures of AA6061 processed by WLSP at 160 $^{\circ}\text{C}$, and corresponding diffraction patterns: (a) T6 sample and (b) solutionized sample.

of dislocations is strongly pinned by precipitates, resulting in the formation of highly diffused dislocation arrangements instead of dislocation slip bands.

To have a better sight on the precipitate structures, selected area diffraction technique is applied to effectively obtain the weak diffraction spots associated with the precipitate structures in the diffraction pattern. The DF TEM image of typical precipitate structures in AA6061-T6 sample after WLSP at 160 $^{\circ}\text{C}$ is shown in Fig. 3(a). This image is taken in the $[-112]$ zone axis by selecting a weak diffraction spot associated with precipitates. The spot is near $(-11-1)$, and is circled and indicated using an arrow as shown in the diffraction pattern. For comparison, the precipitate structures of solutionized AA6061 after WLSP at 160 $^{\circ}\text{C}$ are characterized as shown in Fig. 3(b). It is observed that both rod shape precipitates, around 100 nm in length and spherical shape ones, around 10 nm in diameter exist in the T6 condition sample [Fig. 3(a)], while highly dense spherical-shaped precipitates are mostly presented in the solutionized sample [Fig. 3(b)]. It is generally accepted that three phases of precipitates are generated in Al-Mg-Si alloy with the precipitation sequence: $\beta'' \rightarrow \beta' \rightarrow \beta$, where β'' is needle-shaped growing along $\langle 100 \rangle$ direction with a monoclinic structure, β' is rodlike growing along $\langle 100 \rangle$ direction with a hexagonal crystal structure, and β phase is Mg_2Si platelets on $\{100\}$ of Al with a CaF_2 structure. It is clearly interpreted by Fig. 3 that the rodlike β' phase precipitates are brought by the initial material condition due to the T6 static aging, and the highly dense spherical-shaped precipitates are generated by WLSP

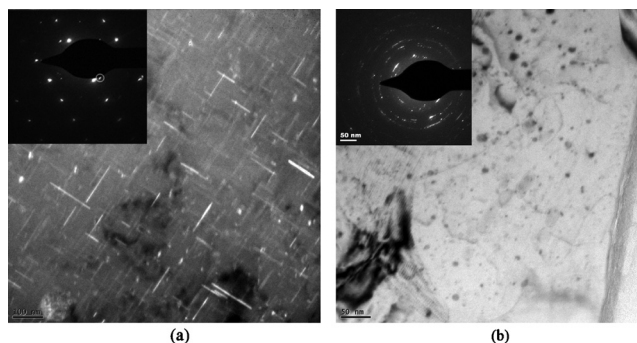


FIG. 3. TEM images showing precipitate structures in AA6061 processed by WLSP at 160 $^{\circ}\text{C}$, and corresponding diffraction patterns: (a) both rod and spherical precipitates in the T6 sample; and (b) spherical precipitates in the solutionized sample.

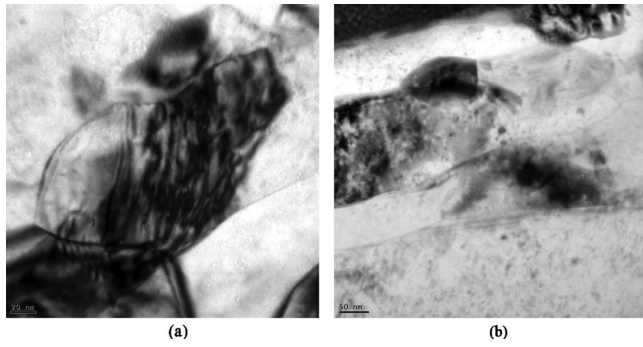


FIG. 4. TEM images showing the density of spherical precipitates in solutionized AA6061 samples processed by: (a) LSP at room temperature and (b) WLSP at 90 °C.

due to the DA. The spherical shape can be explained by the fact that the short DA time is not effective for the precipitate growth.

In order to compare the precipitate density affected by the processing temperature, the bright field TEM images of solutionized AA6061 after (a) LSP at room temperature, (b) WLSP at 90 °C are shown in Fig. 4. It can be seen that the precipitate density of the 160 °C WLSP sample is at the order of magnitude of $10^4/\mu\text{m}^3$ [Fig. 3(b)], which is slightly higher than that of the 90 °C WLSP sample. However, very few precipitates are observed in the room temperature LSP sample. This significant increase in the precipitate density directly demonstrates the effect of the working temperature on the nucleation mechanism during DA.

Therefore, these images ascertain that WLSP generates a unique microstructure with extremely dense precipitates and such high density has not been reported by any other technique.

IV. A NUCLEATION MODEL FOR WLSP

A. Available density of nucleation sites

Because materials' mechanical properties are strongly affected by the density and size distribution of the precipitates generated by WLSP, it is important to investigate the nucleation mechanism during this DA process. DA is an integrated strengthening process combining the thermomechanical processing and aging treatments, which result in a unique microstructure with nanoscale precipitates surrounded by dense dislocation structures. During DA, the nucleation and growth of precipitates are related to the temperature and strain rate,⁸ while in static aging the precipita-

tion is related to the temperature, applied stress and time.⁹ It is also generally accepted that precipitation during DA is dislocation-assisted.¹⁰

The available nucleation site is employed to describe the sites where it is possible for the nucleation to take place. Based on the assumption that the dislocation nodes are the favored nucleation sites for precipitation, the density of available nucleation sites is expressed to be proportional to the dislocation density.^{11,12} With consideration of the effects of strain rate and temperature on the nucleation kinetics, the available nucleation sites density N_0 can be represented as

$$N_0(I_0, T) = \frac{1}{2} \rho_t (I_0, T)^{3/2}, \quad (1)$$

where ρ_t is the total dislocation density, I_0 is the laser intensity, and T is the working temperature.

According to Taylor's classical dislocation model,¹³ the total dislocation density could be given as a function of the flow stress σ

$$\rho_t = \left(\frac{\sigma_d}{M \gamma \mu b} \right)^2 = \left(\frac{\sigma - \sigma_0}{M \gamma \mu b} \right)^2, \quad (2)$$

where M is the Taylor factor (≈ 3.10), μ and b are the shear modulus and Burgers vector of dislocations, γ is a scalar coefficient between 0.2 and 0.4, and the flow stress of metallic materials consists of two components: the friction stress σ_0 and the strength contribution due to dislocation structures σ_d .

To estimate the flow stress after WLSP, the extended mechanical threshold stress (MTS) model is employed,¹⁴ in which the flow stress is considered to have the four components: the athermal component τ_a , the intrinsic component due to barriers to the thermally activated dislocation motion τ_i , the viscous drag component due to viscous drag effects τ_v , and the structure evolution component τ_e

$$\sigma = (\tau_a + \tau_i + \tau_v + \tau_e) \frac{\mu}{\mu_0}, \quad (3a)$$

where μ_0 is the shear modulus at 0 K. τ_i , τ_v , τ_e , and μ related to the strain rate $\dot{\epsilon}$, plastic strain ϵ_p , pressure p , and temperature T are defined as

$$\tau_i(\dot{\epsilon}, T) = \sigma_i \left[1 - \left(\frac{k_b T}{g_0 i b^3 \mu} \ln \frac{\dot{\epsilon}_{0i}}{\dot{\epsilon}} \right)^{1/q_i} \right]^{1/p_i}, \quad (3b)$$

$$\tau_v(\dot{\epsilon}) = \frac{2B\dot{\epsilon}}{\sqrt{3}\rho_m b^2}, \quad (3c)$$

$$\tau_e(\epsilon_p, \dot{\epsilon}, T) = \sigma_{es} \left(\frac{e^{2\theta_0 \epsilon_p / \sigma_{es}} - 1}{e^{2\theta_0 \epsilon_p / \sigma_{es}} + 1} \right) \left[1 - \left(\frac{k_b T}{g_0 e b^3 \mu} \ln \frac{\dot{\epsilon}_{0e}}{\dot{\epsilon}} \right)^{1/q_e} \right]^{1/p_e}, \quad (3d)$$

$$\mu(p, T) = \frac{1}{1 + \exp \left[-\frac{1 + 1/\zeta}{1 + \zeta/(1 - T/T_m)} \right]} \left\{ \left[\mu_0 + p \frac{\partial \mu}{\partial p} \left(\frac{a_1}{\eta^{1/3}} + \frac{a_2}{\eta^{1/3}} + \frac{a_3}{\eta} \right) \right] \left(1 - \frac{T}{T_m} \right) + \frac{\rho}{cm} k_b T \right\}, \quad (3e)$$

where σ_i is the intrinsic component of the MTS, k_b is the Boltzmann constant, g_{0i} and g_{0e} are the normalized activation energy, $\dot{\epsilon}_{0i}$ and $\dot{\epsilon}_{0e}$ are the constant reference strain rates, B is the drag coefficient, ρ_m is the mobile dislocation density, σ_{es} is the saturation value of the structure evolution component of the MTS, θ_0 is the initial hardening modulus, m is the atomic mass, $\eta = \rho/\rho_0$ is the ratio of mass density, T_m is the melting temperature, and p_i , q_i , p_e , q_e , a_1 , a_2 , a_3 , ζ , and c are the material constants.

The extended MTS model is more precise and reliable to simulate WLSP process than other flow stress models. This is due to the following two reasons: (1) MTS model is a physical based model, which takes the dislocation motion and accumulation into account; (2) the extended MTS model integrates the thermally activated dislocation motion and the viscous drag effects, which make the model feasible for the ultra high strain rate deformation (greater than $10^5/s$); while other flow stress models (e.g., Johnson-Cook model) are only practical within a lower strain rate range.

During WLSP process, the plastic strain ϵ_p is determined by the applied laser intensity and the strain rate $\dot{\epsilon}$ varies with time. In order to simplify the calculation, the average strain rate $\dot{\epsilon}(I_0)$ dependent on the laser intensity and the shockwave rising time t_l is utilized and defined as

$$\dot{\epsilon}(I_0) = \frac{\epsilon_p(I_0) + \epsilon_e(I_0)}{t_l} = \frac{\epsilon_p(I_0) + \frac{P(I_0)}{E}}{t_l}, \quad (4)$$

where $\epsilon_p(I_0)$ and $\epsilon_e(I_0)$ present the plastic and elastic strain, and E is Young's modulus.

According to Fabbro's analytical model for LSP,¹⁵ the surface plastic strain related to the peak pulse pressure $P(I_0)$ can be written as

$$\epsilon_p(I_0) = \frac{-2HEL}{3\lambda + 2\mu} \left(\frac{P(I_0)}{HEL} - 1 \right), \quad (5a)$$

$$\lambda = \frac{E\nu}{(1+\nu)(1-2\nu)}, \quad \mu = \frac{E}{2(1+\nu)}, \quad (5b)$$

$$P(I_0) = 0.10 \left(\frac{\alpha}{2\alpha + 3} \right)^{1/2} Z^{1/2} I_0^{1/2}. \quad (5c)$$

Hugoniot elastic limit (HEL) is applied to assess the plastic deformation. During WLSP, the depth of the plastic deformation zone extends to a point at which the peak stress no longer exceeds HEL. λ and μ are Lamé's constants in terms of Young's modulus E and Poisson's ratio ν . The peak pulse pressure is estimated as a function of the shock impedance Z and the laser intensity, where α is the efficiency of the interaction (≈ 0.11).

Thus, the density of the available nucleation sites during WLSP could be calculated as a function of the applied laser intensity and the working temperature. These two variables are directly determined by the WLSP process. However, the available nucleation sites only describe the sites where it is possible for the nucleation to take place. The nucleation rate is also strongly affected by other factors, such as the activation energy.

B. Activation energy and nucleation rate

With the assumptions that dislocation nodes are favored as nucleation sites and the dislocation core energy is spent for the nucleation growth, the activation energy for nucleation in WLSP process consists of four components represented as

$$\Delta G = V(\Delta G_{chem} + \Delta G_\epsilon) + \gamma_i - \Delta G_d, \quad (6)$$

where V is the volume of nucleus, ΔG_{chem} , ΔG_ϵ , γ_i , and ΔG_d are the chemical driving force, volume strain energy, interfacial free energy, and dislocation core energy relatively.¹⁶

The chemical driving force ΔG_{chem} represents the excess free energy provided by the unstable phase relative to the stable phase. It depends on the equilibrium concentration of precipitate forming elements. As discussed in Dutta's precipitation model,^{11,12} ΔG_{chem} of the Mg_2Si precipitate in AA6061 could be expressed as

$$\Delta G_{chem} = \frac{R_g T}{V_m} \ln \frac{C_{Mg} C_{Si}}{C_{Mg}^e C_{Si}^e}, \quad (7)$$

where R_g is the universal gas constant, T is the isothermal annealing temperature, V_m is the molar volume of the species, C_{Mg} and C_{Si} are the instantaneous concentrations of Mg and Si in mol fractions, as well as C_{Mg}^e and C_{Si}^e are the equilibrium concentrations at the annealing temperature.

The volume strain energy (ΔG_ϵ) is associated with the lattice mismatch between precipitates and the metal matrix. It is strongly influenced by several factors including the mechanical properties, the lattice disregistry δ , and the coherency loss parameter C . It could be defined as^{17,18}

$$\Delta G_\epsilon = f(\mu_{Al}, \mu_p, \nu_{Al}, \nu_p) (\delta_e^3 + 3\delta_e^2 + 3\delta_e)^2, \quad (8a)$$

$$\delta = \delta_e + \delta_p, \quad C = \delta_p / \delta, \quad (8b)$$

where f is a function dependent on the shear modulus and Poisson's ratio of precipitates (μ_p, ν_p) and AA6061 matrix (μ_{Al}, ν_{Al}), and δ_e and δ_p are the elastic and plastic lattice disregistry.

Interfacial free energy (γ) represents the work of the formation of the interface between the precipitate and the matrix. It is defined by Eq. (9), where S and $\gamma_{\alpha\beta}$ are the surface area and surface energy of nucleus

$$\gamma_i = S \times \gamma_{\alpha\beta}. \quad (9)$$

The dislocation core energy is related to the minimum critical radius for the stability and the nucleation growth R_c , which is assumed to be equal to the radius of dislocation nodes. It can be expressed as^{11,12,17}

$$\Delta G_d = 0.4\mu b^2 R_c, \quad (10)$$

$$R_c = \frac{2\gamma_{\alpha\beta}}{\Delta G_{chem}}. \quad (11)$$

The nucleation rate is obtained from the classical theory of nucleation as^{19,20}

$$\frac{dN}{dt} = \lambda(T) \times N_0, \quad (12a)$$

TABLE I. Material parameters and data for AA6061 alloy (Refs. 2, 3, 11, 12, 14, and 21).

ν	0.33	τ_a (MPa)	10
HEL (GPa)	0.6	σ_i (MPa)	366.6
E (GPa) at room temperature	70	b (m)	2.86×10^{-10}
E (GPa) at 80 °C	67	k_b (J/K)	1.38×10^{-23}
E (GPa) at 150 °C	64	g_{0i}	0.59
E (GPa) at 200 °C	62	$\dot{\epsilon}_{0i}$ (s ⁻¹)	5.0×10^8
t_i (ns)	20	q_i	1.0
μ_0 (GPa)	31.3	p_i	0.75
σ_{es} (GPa) at room temperature and 80 °C	0.16	g_{0e}	3.0
σ_{es} (GPa) at 150 °C and 200 °C	0.17	$\dot{\epsilon}_{0e}$ (s ⁻¹)	1.0×10^9
ζ	0.1	q_e	1.0
p (GPa)	52.67	p_e	0.75
$\partial\mu/\partial p$	1.8	θ_0 (GPa) at room temperature	2.7
ρ (kg/m ³)	2850	θ_0 (GPa) at 80 °C	2.3
ρ_0 (kg/m ³)	2700	θ_0 (GPa) at 150 °C	2.0
T_m (K)	855	θ_0 (GPa) at 200 °C	1.7
m (amu)	26.98	B (Pa s)	0.1×10^{-4}
a_1	0.53	ρ_m (m ⁻²)	1×10^{13}
a_2	0.10	c	0.049
a_3	0.37	γ	0.2
μ (GPa) at room temperature	26.7	M	3.1

$$\lambda(T) = Z' \beta' \exp\left(-\frac{\Delta G}{kT}\right) \exp\left(-\frac{\tau}{t}\right), \quad (12b)$$

where N is the number of precipitates per unit volume, $\lambda(T)$ is the nucleation coefficient (between 0 to 1) affected by the processing temperature, Z' is Zeldovich's factor, and t and β' is the time and atomic impingement rate. The incubation period τ can be assumed zero since the precipitation on the dislocations is instantaneous.

V. RESULTS AND DISCUSSION

In WLSP, the enhanced mechanical properties including hardness and fatigue life are resulted from the generation of nanoscale precipitates. Here, the developed nucleation model will be used to predict the nucleation rate as a function of processing conditions and understand the mechanism of the nucleation process. The parameters of AA6061 used for the calculation are given in Table I.^{2,3,11,12,14,21}

Figure 5 shows the simulation results of the flow stress

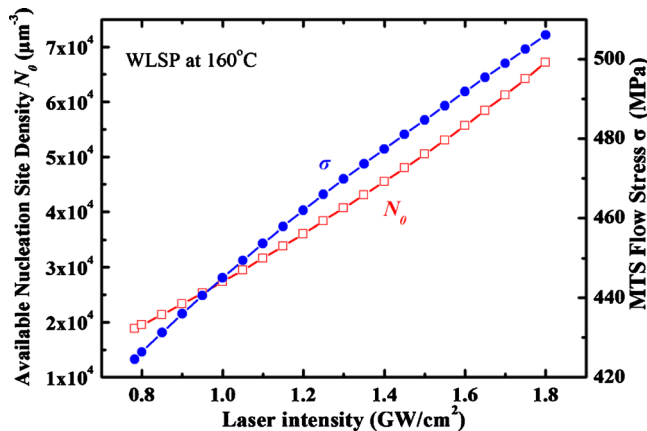


FIG. 5. (Color online) The density of available nucleation sites and MTS flow stress vs the laser intensity, simulated by the nucleation model.

[Eq. (3)] and the density of available nucleation sites [Eq. (1)] of AA6061 after WLSP at 160 °C, which are increased by enhancing the laser intensity. It can be seen that while raising the laser intensity from 0.8 to 1.6 GW/cm², the flow stress has a 15% increase from around 425 to 490 MPa. This increase is due to the higher strain rate processing related to the higher laser intensity. It is also found that the order of magnitude of the available nucleation site density is 10⁴/μm³, which is much higher than that generated by conventional material processing techniques with smaller strain rates, such as forging, extrusion, and rolling (normally 10¹–10³/μm³).²²

Figure 6 illustrates the temperature effect on the nucleation coefficient [Eq. (12)]. The Y-axis represents the logarithm of the ratio of the nucleation coefficient at temperature T to that at room temperature. The activation energy of nucleation is taken to be 10⁻¹⁷ J, which is chosen based on the reported order of magnitude.¹¹ It can be seen that the nucleation coefficient is dramatically increased by elevating

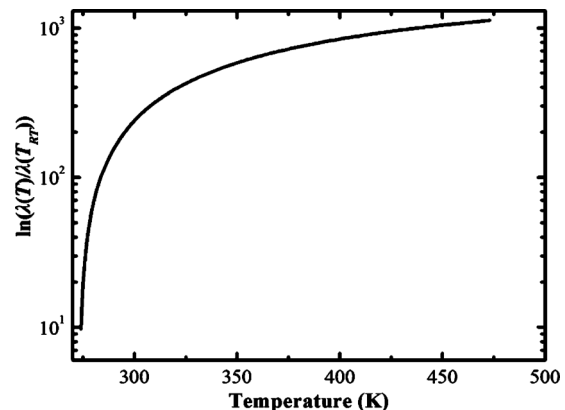


FIG. 6. The effect of working temperature on the nucleation coefficient. The Y-axis represents the logarithm of the ratio of nucleation coefficient at temperature T to that at room temperature.

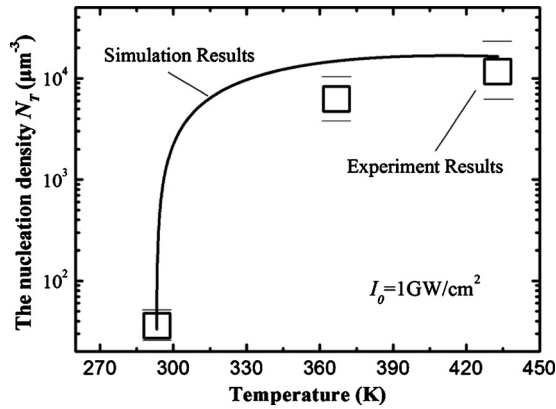


FIG. 7. Comparison of experimental and simulation results on the nucleation density affected by WLS processing temperature.

the working temperature. For instance, the nucleation coefficient at 160 °C is almost e^{1000} times greater than that at room temperature.

Figure 7 shows a comparison of the predicted nucleation density with the experimental results from TEM images. Each experimental point is obtained from the average of five measurements. Both simulation and experimental results show that the nucleation density of AA6061 after WLS at 160 and 90 °C has the order of magnitude of 10^4 and $10^3/\mu\text{m}^3$ relatively, while LSP at room temperature could hardly generate precipitates. Therefore, it can be concluded that the model shows a good agreement with the experiment data.

In this study, the full width at half maximum (FWHM) of 2θ measured by XRD (Bruker D8-Discover Superspeed) is used to compare the relative defect density.^{23,24} Figure 8 shows the FWHM of 2θ versus the laser intensity for LSP and WLS at various processing temperatures. It can be seen that both the elevated processing temperature and the enhanced laser intensity result in a greater FWHM value, which represents a higher defect density. This could be mainly due to the formation of the highly dense and diffused nanoprecipitates during WLS, which hinder dislocation slip by the pinning mechanism and result in a higher dislocation density. Figure 9 shows the simulated defect volume density combining the volume density of dislocations [Eq. (2)] and precipi-

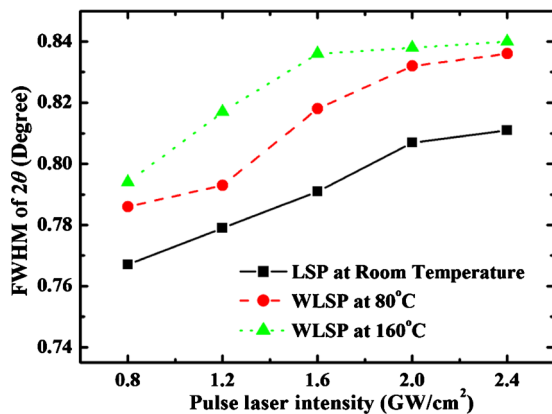


FIG. 8. (Color online) FWHM of 2θ vs WLS temperature and laser intensity.

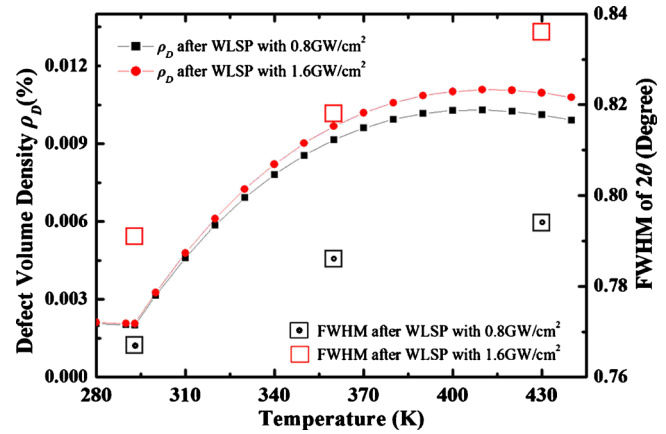


FIG. 9. (Color online) Simulated defect volume density increased with laser intensity and WLS working temperature.

tates [Eq. (12)]. It is observed that the defect volume density is increased with the processing temperature and the laser intensity of WLS. This trend agrees with the experimental results in Fig. 8.

As discussed above, both experimental and simulation results have indicated that the precipitation and nucleation growth during WLS is assisted and accelerated by: (1) the high strain rate deformation and the resulted high dislocation density, and (2) the elevated working temperature. This can be explained by the three following reasons, which could strongly affect the activation energy of nucleation

- (1) The strain energy for precipitation caused by the mismatch between two lattices is decreased by the presence of highly dense dislocations. Without the highly dense dislocations generated by WLS, the matrix/precipitate interface is partially coherent or even fully coherent [Fig. 10(a)], which means the lattice disregistry δ is mainly balanced by the elastic straining; on the contrary, while the precipitates are surrounded by highly dense dislocations, the matrix/precipitate interface is semicoherent, and the lattice disregistry is accommodated by both the elastic straining and the edge dislocations [Fig. 10(b)].^{17,20} According to Eq. (8), if the coherency loss parameter C is increased from 5% to 50% after WLS, the volume strain energy could be reduced by 86.25%. Thus, the lower elastic lattice disregistry δ_e induced by the higher dislocation density reduces the activation energy of nucleation by decreasing the strain energy for the lattice mismatch.

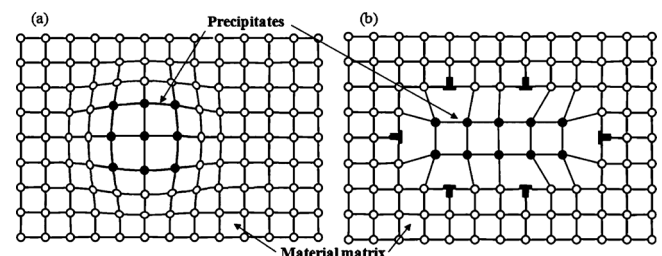


FIG. 10. Matrix/precipitate lattice disregistry. (a) matrix/precipitate interface is coherency; and (b) matrix/precipitate interface is semicoherency (Ref. 20).

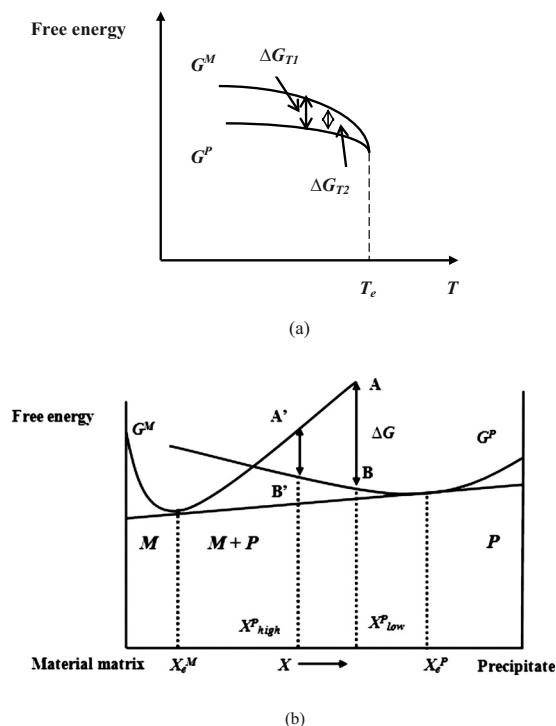


FIG. 11. The chemical driving force dependent on the working temperature and the material matrix/precipitate concentrations.

- (2) The chemical driving force for precipitation is reduced by elevating the working temperature of WLSP. Figure 11 illustrates the chemical driving force for precipitation affected by the working temperature [Fig. 11(a)] and matrix/precipitate concentrations [Fig. 11(b)], where ΔG_T stands for the chemical driving force at temperature T , G^M and G^P are the free energy of matrix material and precipitate, and X^M and X^P are the concentration of matrix material and precipitate.^{16,25} Since the chemical driving force for nucleation represents the excess free energy provided by the unstable phase relative to the stable structure, it could be expressed as the vertical distance between the matrix and precipitate free energy curves ($G^M - G^P$). As shown in Fig. 11(a), a precipitate is generally considered as the relatively stable phase with lower free energy before reaching the equilibrium temperature T_e , and the excess free energy provided by the unstable phase (matrix material) is reduced by elevating the temperature. This results in a lower chemical driving force at a higher working temperature. On the other hand, since the precipitation reaction is an endothermic solid phase reaction, a higher temperature could generate a greater precipitate concentration in the matrix/precipitate solid solution. As illustrated in Fig. 11(b), increasing precipitates concentration from X^{low} to X^{high} could cause a smaller free energy difference ($|A'B'| < |AB|$), which means a lower chemical driving force for the precipitation. This could also be understood by Eq. (7) that the elevated working temperature could decrease the instantaneous concentrations of precipitate elements in the solid solution, and result in a reduced chemical driving force.
- (3) The activation energy is reduced by enhancing the dis-

location core energy due to the higher dislocation density. During the WLSP process, the mechanical energy provided by the laser-induced plasma is spent to create both dense mobile dislocation structures and the dislocation nodes. This energy is partially stored in dislocation nodes and will be released during the precipitation for the nucleation growth, resulting in a lower requirement of the external applied energy for nucleation. In addition, the higher dislocation density generated by WLSP stimulates stronger dislocation interactions to form the longer radius of dislocation nodes. That indicates that a higher dislocation core energy is stored [Eq. (10)]. For instance, if the dislocation core radius in AA6061 grows from 0.5 to 1 nm, the dislocation core energy is enhanced from 4.9×10^{-19} to 10^{-18} J. It can be also explained by Eq. (11) that the critical radius for the stability and the nucleation growth R_c grows longer due to the reduction in the chemical driving force caused by the elevated working temperature as discussed in reason (1).

VI. CONCLUSIONS

In this study, AA6061 has been processed by WLSP, and its microstructure morphologies after processing have been characterized by TEM; the WLSP nucleation model has been proposed to do the quantitative analyses; the effects of the elevated working temperature and dense dislocation structures on the nucleation growth have been discussed. The results have drawn following remarks:

- (1) a unique microstructure with highly dense nanoscale precipitates surrounded by dense dislocation structures is generated by WLSP;
- (2) during WLSP, the precipitation reaction occurs simultaneously during the deformation process due to the DA;
- (3) the warm temperature of WLSP has a favorable influence on the nucleation rate by decreasing the chemical driving force of the precipitation;
- (4) the high dislocation density introduced by the deformation assists and accelerates the nucleation growth due to the lower volume strain energy and the higher dislocation core energy.

We envision that WLSP can be served as an innovative thermomechanical processing and a DA technique which brings the beneficial microstructures to metallic materials for industrial applications.

ACKNOWLEDGMENTS

The authors appreciate the support from Office of Naval Research (ONR) through Young Investigator Program. This work is also partially supported by NSF under Grant No. CMMI 0900327.

- ¹I. Nikitin, B. Scholtes, H. J. Maier, and I. Altenberger, *Scr. Mater.* **50**, 1345 (2004).
- ²C. S. Montross, T. Wei, L. Ye, G. Clark, and Y. W. Mai, *Int. J. Fatigue* **24**, 1021 (2002).
- ³K. Ding and L. Ye, *Laser Shock Peening: Performance and Process Simu-*

- lation (Woodhead, Cambridge, 2009).
- ⁴A. Wick, V. Schulze, and O. Vohringer, *Mater. Sci. Eng., A* **293**, 191 (2000).
- ⁵S. Gündüz, *Ironmaking Steelmaking* **29**, 341 (2002).
- ⁶H. F. Jiang, X. D. Chen, Z. C. Fan, J. Dong, H. Jiang, and S. X. Lu, *J. Nucl. Mater.* **392**, 494 (2009).
- ⁷C. Ye, Y. L. Liao, and G. J. Cheng, *Adv. Eng. Mater.* **12**, 291 (2010).
- ⁸I. Alvarez-Armas and S. Hereñú, *J. Nucl. Mater.* **334**, 180 (2004).
- ⁹A. W. Zhu, J. Chen, and E. A. Starke, *Acta Mater.* **48**, 2239 (2000).
- ¹⁰M. Cai and G. J. Cheng, *JOM* **59**, 58 (2007).
- ¹¹B. Dutta, E. Valdes, and C. M. Sellars, *Acta Metall. Mater.* **40**, 653 (1992).
- ¹²B. Dutta, E. J. Palmiere, and C. M. Sellars, *Acta Mater.* **49**, 785 (2001).
- ¹³G. I. Taylor, *J. Inst. Met.* **62**, 307 (1938).
- ¹⁴B. Banerjee and A. S. Bhawalkar, *J. Mech. Mater. Struct.* **3**, 391 (2008).
- ¹⁵R. Fabbro, J. Fournier, P. Ballard, D. Devaux, and J. Virmont, *J. Appl. Phys.* **68**, 775 (1990).
- ¹⁶D. A. Porter and K. E. Easterling, *Phase Transformations in Metals and Alloys* (CRC, Boca Raton, FL, 2009).
- ¹⁷W. J. Liu and J. J. Jonas, *Mater. Sci. Technol.* **5**, 8 (1989).
- ¹⁸J. D. Eshelby, *Proc. R. Soc. London, Ser. A* **241**, 376 (1957).
- ¹⁹R. Wagner and R. Kampmann, *A Comprehensive Treatment* (VCH, Germany, 1991).
- ²⁰K. C. Russell, *Adv. Colloid Interface Sci.* **13**, 205 (1980).
- ²¹J. R. Davis and A. I. Handbook Committee, *Metals Handbook* (ASM International, Materials Park, Ohio, 1998).
- ²²S. Kalpakjian and S. R. Schmid, *Manufacturing Engineering and Technology* (Prentice-Hall, New Jersey, 2009).
- ²³Y. S. Park, K. H. Kim, J. J. Lee, H. S. Kim, T. W. Kang, H. X. Jiang, and J. Y. Lin, *J. Mater. Sci.* **39**, 1853 (2004).
- ²⁴V. M. Kaganer, R. Kohler, M. Schmidbauer, R. Opitz, and B. Jenichen, *Phys. Rev. B* **55**, 1793 (1997).
- ²⁵H. K. Hardy and T. J. Heal, *Mech. Phase Transform. Met.* **18**, 1 (1955).